


RESEARCH ARTICLE

Quantum-Enhanced Optomechanical Sensor Network

Qinghui Li¹ | Wei Li^{1,2} | Yufan Wang¹ | Yajun Wang^{1,2} | Long Tian^{1,2} | Shaoping Shi^{1,2} | Yaohui Zheng^{1,2} ¹State Key Laboratory of Quantum Optics Technologies and Devices, Institute of Opto-Electronics, Shanxi University, Taiyuan, China | ²Collaborative Innovation Center of Extreme Optics, Shanxi University, Taiyuan, ChinaCorrespondence: Wei Li (xliwei@sxu.edu.cn) | Yaohui Zheng (yhzheng@sxu.edu.cn)

Received: 26 June 2025 | Revised: 23 October 2025

Keywords: distributed quantum sensing | optomechanical sensor network | quantum metrology

ABSTRACT

Distributed quantum sensing (DQS), an essential branch of quantum metrology, can substantially boost the sensitivity and reliability in multi-parameter estimation, achieving the Heisenberg scaling. Here, we report the first experimental demonstration of a quantum-enhanced optomechanical sensor network, achieving the DQS advantage of a maximum \sqrt{M} -fold increase trend with sensor number. The challenge of poor uniformity is addressed by decoupling and independently manipulating each optomechanical parameter, and the acquired inconsistencies are less than 2.4%. By tailoring a four-partite entangled state, the acquired quantum advantage is 57.3% compared to that with coherent probes, and 23.7% compared to that with the separable scheme. Moreover, the quantum enhanced optomechanical sensor network is applied to estimate incoherent forces, enhancing the estimation resolution by 33.7% in contrast with the separable scheme. The entanglement-enhanced optomechanical sensors with high consistency pave the way for future large-scale quantum sensor network, facilitating the micro-seismic epicenter locating, dark matter searching, and so on.

1 | Introduction

Quantum metrology [1, 2] offers a remarkable opportunity to improve the sensitivity of parameter estimation beyond the standard quantum limit by leveraging quantum characteristics such as squeezing or entanglement, squeezing and superposition, providing access to the Heisenberg limit that is available in no other way [3–5]. Exploiting the unique properties of diverse physical systems, including atomic ensembles [6], solid-state spin [7], optomechanical [8], ultracold atoms [9] and molecules [10], the combination of advances in material and control techniques continues to enhance measurement precision of individual sensors [11, 12]. Especially, by externally injection of a single-mode squeezed state [13], the sensitivities have been improved in gravitational wave detection [14–16], magnetometer [17], biological imaging [18] and force sensing [19–21]. The measurement sensitivity can also be enhanced by generating intrinsic squeezing in a crystal sphere [22] and optomechanical systems [23–30].

Nevertheless, individual quantum sensor excels in localization and high-sensitivity tasks, but faces critical limitations in scalability, target positioning, and multi-parameter sensing. Quantum sensor network that addresses many of these limitations of individual quantum sensor combines distributed sensors with shared quantum resources to achieve unprecedented sensing sensitivity and reliability, positioning resolution, undoubtedly promoting conceptual advances and technical progress of disaster warning [31–34], resource exploration and military defense [35].

Distributed quantum sensing (DQS) [36, 37], a sensing protocol where multiple sensors share the continuous variable (CV) multipartite entangled state produced from one squeezed state, can achieve the Heisenberg scaling in the noiseless condition, thereby enabling a measurement precision scales inversely with the number of sensors [38–43]. Relying on the sensor number and the weights of CV multipartite entangled state [44], researchers have demonstrated quantum advantage in numerous

distributed sensing problems including radio-frequency signals [44–46] and optical phase [47]. Recently, enhanced precision in a clock network has been achieved through spatially distributed entanglement in an atomic ensemble [48]. There is no doubt at all that a greater number of sensors enriches the physics of distributed sensing [49–53], up to enough sensors for these applications ranging from gravity-based subterranean imaging to dark matter searches [54]. One of the main limitations of scaling the sensor network is quantum decoherence from system loss, where the quantum advantage can be reinstated via quantum repeaters [55] and quantum error correction [56, 57]. It should be emphasized that almost all demonstrations above employ electro-optic modulators as quantum transducers to simulate multiple physical quantities. Although the sensitivity advantage has been demonstrated using the simulated signal, it has not yet been validated in a more practical scenario. Cavity optomechanical sensor [8, 58, 59], one of the most accurate, stable, and practical sensors, has facilitated high-precision estimation for numerous physical quantities including gravitational wave [60–62], displacement [63], acceleration [64–66], mass [67], and magnetic field [68, 69]. Recently, researchers have taken a critical step toward integrating arrayed optomechanical sensors with a two-partite entangled state [19]. Looking forward, expanding the optomechanical sensor array can enhance the measurement capabilities and verify many theoretical predictions. However, the optomechanical sensor network with more than two sensors remains largely unexplored.

Here, we report the first experimental demonstration of the quantum-enhanced optomechanical sensor network with a four-partite entangled state shared by four independent optomechanical sensors, demonstrating the DQS advantage of a maximum \sqrt{M} -fold increase trend with sensor number. Starting from an optomechanical sensor model, we construct four optomechanical sensors with the maximum inconsistency of 2.4% [70] by decoupling and independently manipulating single-photon optomechanical coupling strength g_0 , resonator decay rate κ , mechanical decay rate Γ , etc. The work demonstrates a pathway of constructing more consistent optomechanical sensors, enabling new capabilities for a large-scale optomechanical sensor network, facilitating these applications of micro-seismic epicenter [71–73], inertial navigation [74], and dark matter searching [54, 75].

2 | Theoretical Analysis

Figure 1a is a schematic diagram of the quantum-enhanced optomechanical sensor network. Each sensor is composed of a membrane-based mechanical oscillator, whose displacement $x_j(\omega)$ ($j = 1, 2, \dots, m$) is magnified through the interaction between probe and sensor. The membrane displacement is dispersively coupled to the resonant frequency of a resonator, converting it into phase modulation of the probe. The desired force information can be derived by $F_j(\omega) = x_j(\omega)/\chi_j(\omega)$ (see Supporting Information Section S3), where $\chi_j(\omega) = \frac{1}{m_j(\Omega_j^2 - \omega^2 + i\Gamma_j\omega)}$ is mechanical susceptibility, m_j is the effective mass, Ω_j is mechanical resonance frequency, and Γ_j is mechanical decay rate. The force power spectral density (PSD) of a membrane-based optomechanical

sensor can be formulated as

$$S_{F,j}(\omega) = S_{th,j} + \frac{\kappa_j^2 S_{det,j}}{32g_{0,j}^2 \alpha_j^2 |\chi_j(\omega)|^2}. \quad (1)$$

The first term $S_{th,j} = 2\Gamma_j m_j k_B T$ characterizes the thermal noise from Brownian motion, in which k_B is Boltzmann's constant, and T is the bath temperature. The second term represents measured imprecision noise, where $S_{det,j}$ is the quantum fluctuation of phase quadrature for either individual or joint readout processing, and α_j^2 is the input mean photon number. Obviously, the imprecision noise is dependent upon resonator decay rate κ_j and single-photon optomechanical coupling strength $g_{0,j}$, both of which simultaneously (non-independently) change with the resonator length. What is worse, the variation of mechanical decay rate Γ_j can be nonlinearly coupled into the mechanical susceptibility $\chi_j(\omega)$, resulting in the great challenge of fabricating sensors with uniform performance.

Figure 1b illustrates the noise budget of force resolution $\sqrt{S_{F,j}(\omega)}$ at different measurement frequencies. Due to the imprecision noise scales inversely with the squared modulus of susceptibility $\chi_j(\omega)$, it exhibits a resonant enhancement at Ω_j with $\chi_j(\Omega_j) = \frac{1/m_j}{i\Gamma_j\Omega_j}$. At resonance frequency, thermal noise dominates the noise budget and it restricts the acquired minimum force resolution. At off-resonance frequencies, the mechanical susceptibility $\chi_j(\omega)$ becomes sharply suppressed, and the imprecision noise dominates in the total noise budget. The thermomechanical limit, defined as the frequency-independent but temperature-dependent fundamental boundary, is achieved when imprecision noise equals thermal noise contributions. At a cryogenic temperature of 60 mK, the force resolution reaches the thermomechanical limit at the resonant frequency, as shown by the yellow dashed line. However, owing to the intrinsic nature of mechanical susceptibility, achieving the thermomechanical limit far from resonance is exceptionally challenging.

Figure 1c represents the force resolution as a function of mechanical decay rate Γ_j at both resonant (blue curve) and off-resonant (red curve) frequencies. The force resolution improves significantly due to a reduced mechanical decay rate at resonance, and thus cryogenic cooling can effectively improve the minimum force resolution. Figure 1d showcases the force resolution as a function of optomechanical coupling strength $g_{0,j}$. At off-resonance, the force resolution improves with stronger optomechanical coupling, whereas the on-resonant resolution is independent of coupling strength. Moreover, the optomechanical coupling strength $g_{0,j}$ scales inversely with the resonator length ($g_{0,j} \propto L_j^{-1}$), thus a compact resonator can improve the off-resonant force resolution. Alternatively, by introducing a phase-squeezed state, the effective single photon optomechanical coupling strength $g_{0,j}e^{-r}$ can be enhanced by increasing the squeezing parameter r . Figure 1e shows the relationship between force resolution and resonator decay rate κ_j . Apparently, the force resolution at off-resonance can be improved by decreasing the resonator decay rate, which is achieved by increasing the reflectivity of the membrane.

Considering the design parameters of our optomechanical sensor, including resonator length $L = 0.5$ mm, $\kappa/2\pi = 60$ GHz, $\Omega_L/2\pi =$

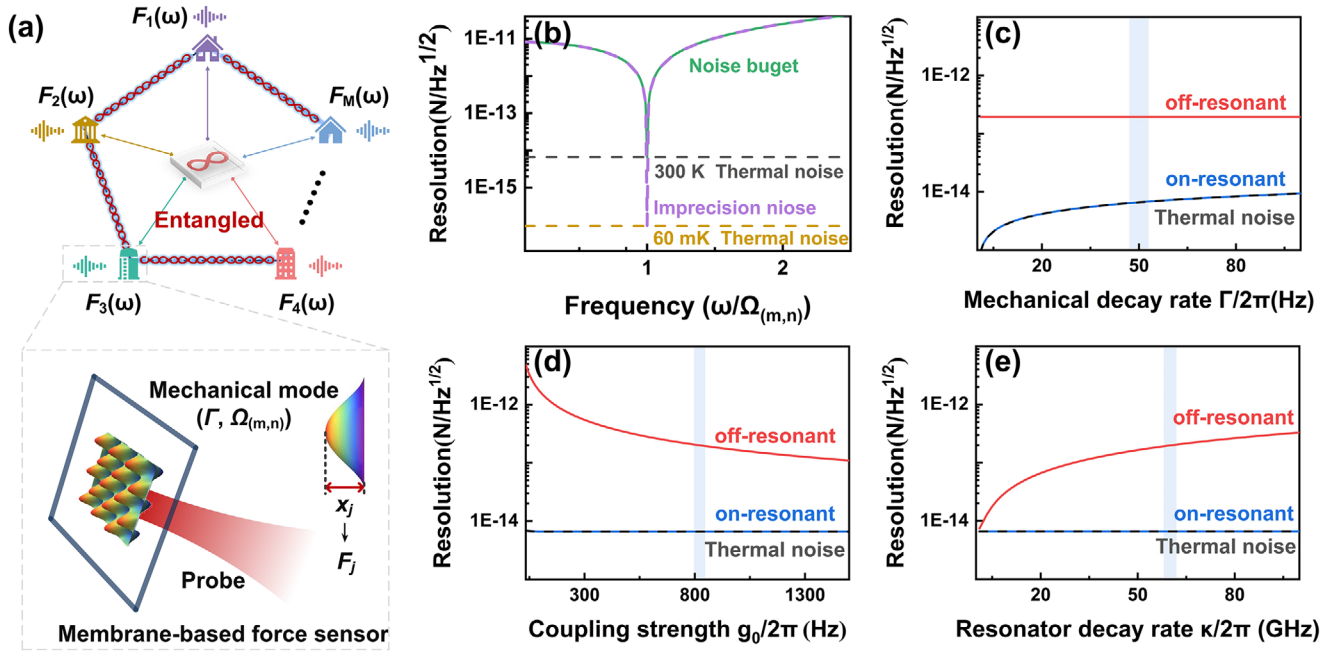


FIGURE 1 | Distributed quantum sensing proposal. Illustration of the entangled network for membrane-based optomechanical sensors (a). Noise budget for force resolution at different measurement frequencies (b), where the green solid curve represents the total noise, the purple, black, and yellow dashed curves correspond to the imprecision noise, thermal noise at 300 K, and thermal noise at 60 mK, respectively. Force resolution versus mechanical decay rate (c), single-photon optomechanical coupling strength (d), and resonator decay rate (e). The red and blue curves show force resolutions for the off-resonant and on-resonant frequencies. The blue shaded regions represent the parameter inconsistency ranges corresponding to a 3% resolution inconsistency.

1.9×10^{14} Hz, $\Gamma/2\pi = 50$ Hz, $g_0/2\pi = 822$ Hz, the force resolution reaches $6.6 \text{ fN Hz}^{-1/2}$ at resonant frequency. In contrast to two optomechanical sensors [19], it is indispensable to guarantee the resolution consistency of all optomechanical sensors. Nevertheless, it is impossible to make two identical sensors due to the slight discrepancies of membranes and mirrors. The inconsistency δ for each parameter X_j can be defined as

$$\delta \sqrt{S_F(\omega, X_j)} = \frac{\left| \sqrt{S_F(\omega, X_j)} - \sqrt{S_F(\omega, X)} \right|}{\sqrt{S_F(\omega, X)}} \quad (2)$$

where parameter X denotes the design value for Γ , g_0 , and κ , while parameter X_j corresponds to the experimentally measured value. To achieve a resolution inconsistency of less than $\pm 3\%$, each parameter, including the resonator decay rate κ , the mechanical decay rate Γ and the single-photon optomechanical coupling strength g_0 , should be finely manipulated to avoid the intercoupling. At the resonance frequency, the lower bound of the force resolution is limited by the thermal noise. Therefore, we mainly focus on the manipulation of the mechanical decay rate Γ to decrease the discrepancy between sensors, by tuning the size and position of the probe on the membrane. At off-resonance frequencies, the resonator decay rate κ and single-photon optomechanical coupling strength g_0 dominate the force resolution, which is manipulated by only displacing resonator length under the premise of not sacrificing consistency at the resonance point. The inconsistency ranges are $\pm 6.0\%$ for the mechanical decay rate, $\pm 3.0\%$ for optomechanical coupling strength, and $\pm 3.0\%$ for the resonator decay rate, as indicated by the blue

shadow in Figure 1c–e. Achieving such consistency is crucial, as even small variations of these parameters can significantly impact the overall force resolution, leading to deviations that could undermine the measurement reliability. The entangled sensor network integrating consistent quantum sensors can be conveniently expanded to large-scale metrological applications.

3 | Experimental Diagram

Figure 2 illustrates the experimental setup of an optomechanical sensor network. A phase squeezed state is generated by a sub-threshold doubly resonant optical parametric amplifier (DROPA) operating in parametric amplification condition [76–79]. The four-partite entangled state is generated by dividing the phase squeezed state with a beam splitter network (BSN), while the weight for each submode can be controlled by a combination of half wave plate and polarization beam splitter (PBS). Compared to other complex proposals to generate multipartite entanglement [80–82], this approach has been demonstrated as the optimal strategy for achieving the ultimate quantum advantage in distributed sensing [44, 45, 47, 83]. The maximum four-partite entangled state is produced with BSN splitting ratios of 25:75, 33:67, and 50:50 respectively, as proved in Supporting Information Section S1. Each submode is converged to a waist radius of $72 \mu\text{m}$ to drive a membrane-based optomechanical sensor. The desired force information of the membrane is encoded in the phase quadrature of the reflected submode, which is extracted by a PBS and a quarter wave plate (QWP). To maximize the extraction efficiency, the polarization of the reflected submode is completely vertical to that of the injected submode by regulating the angle

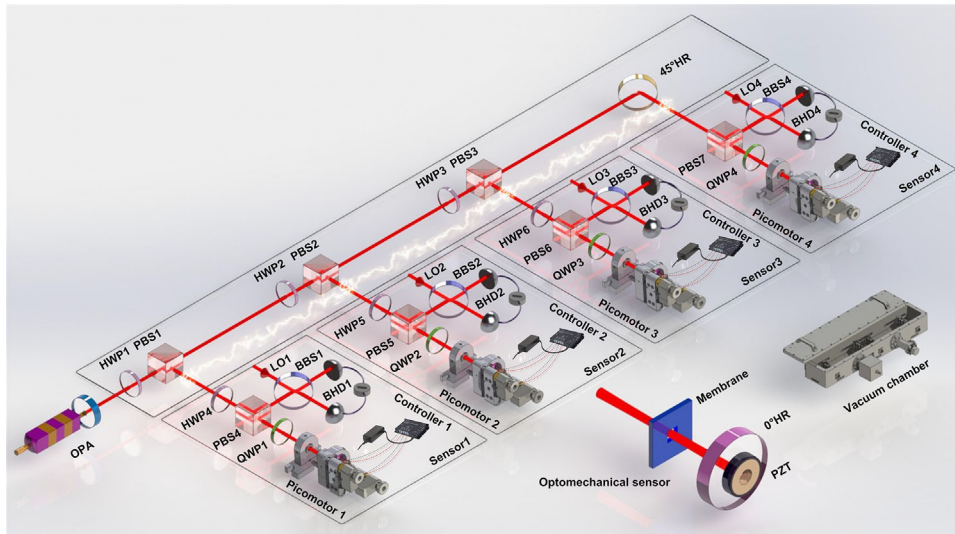


FIGURE 2 | Schematic diagram of the experimental setup. OPA: optical parametric amplifier; HWP: half wave plate; PBS: polarization beam splitter; QWP: quarter-wave plate; BBS: balanced beam splitter; LO: local oscillator; BHD: balanced homodyne detector; 0° (45°) HR: 0° (45°) high reflectivity mirror; PZT: piezoelectric transducer.

of QWP. The reflected submode is then interfered with a strong local oscillator on a balanced beam splitter, and the output beams are measured by a high-efficiency balanced homodyne detector (BHD). The maximum desired force information encoded in phase quadrature is acquired by locking the relative phase between the strong local oscillator and weak probe to $\pm\pi/2$. Any deviation from this specific phase decreases the signal-to-noise ratio due to the noise coupling between the amplitude and phase quadratures. The joint PSDs are obtained by summing the AC component of BHDs (see Supporting Information Section S5) from the whole optomechanical sensors and recorded by a spectrum analyzer. The separable scenario ($M = 1$) is achieved by removing the BSN and driving the membrane-based optomechanical sensor with an individual squeezed state that has an identical photon number.

Each optomechanical sensor is composed of a 0° high reflectivity mirror and a silicon nitride (Si_3N_4) membrane with transverse (drum) vibrations driven by thermal Brownian fluctuations. The consistency of four optomechanical sensors is guaranteed via independent manipulation of resonator decay rate κ , single-photon optomechanical coupling strength g_0 , and mechanical decay rate Γ . The pitch and yaw degrees of freedom for each 0° HR mirror are manipulated by picomotor actuators and controllers, ensuring exact alignment for each sensor. Additionally, a piezoelectric transducer is mounted on the back of the 0° HR mirror to control the length of the membrane resonator. The free spectral ranges are used to calibrate the resonator lengths of four optomechanical sensors. Following this calibration, the resonator decay rates of four sensors are determined by the membrane reflectivities. Moreover, four sensors have adjacent resonator decay rate κ , which is much larger than Ω_j , satisfying the bad cavity (non-resolved sideband) condition that maximizes optomechanical information transfer to the probe light. By controlling the incident power of each sensor, a similar resonator-enhanced optomechanical coupling strength is achieved. To guarantee the similar mechanical decay rate Γ , each Si_3N_4 membrane is bonded to the same stable holder with three corners, minimizing the

contact area to reduce acoustic impedance and radiation losses. Furthermore, the membrane-based optomechanical sensor network is arranged in a vacuum chamber operating at pressures below 10^{-6} Torr to reduce gas damping.

4 | Experimental Results

4.1 | Entanglement-Induced Imprecision Noise Reduction

In the separable scenario, each optomechanical sensor is driven by an independently prepared squeezed state with average photon number $n_s = N_s/M$. With a $5 \mu\text{W}$ probe laser, the back-action noise ($9.7 \times 10^{-22} \text{ N Hz}^{-1/2}$) [84] is negligible compared to the thermomechanical noise ($6.6 \times 10^{-15} \text{ N Hz}^{-1/2}$). Figure 3a-d depicts the independent PSD for each optomechanical sensor. The black curves indicate the normalized shot noise limit (SNL), which is a fundamental bound stemming from the uncertainty relation between the conjugate amplitude quadrature \hat{X} and phase quadrature \hat{Y} . The blue curves represent the squeezing enhanced measurements for the (5,6) mechanical modes of the membranes. The observed resonance frequencies of four optomechanical sensors are 4.276, 4.301, 4.338, and 4.365 MHz, respectively, which coincide with the theoretical predictions. At the off-resonant frequencies, the imprecision noise that dominates the noise budget is reduced by ≈ 0.8 dB below the SNL by harnessing an individual squeezed probe. Thanks to the rigorous manipulation of three pivotal parameters, the consistency of four optomechanical sensors can be manifested from the amplitude and linewidth of the measured mechanical modes.

The maximum four-partite entangled state is customized by quartering the phase squeezed state with an average photon number N_s , yielding four submodes with an average photon number $n_s = N_s/M$. Each submode drives an optomechanical sensor, guaranteeing synchronized membrane vibration amplitudes. Figure 3e showcases the joint homodyne PSD obtained by superposing

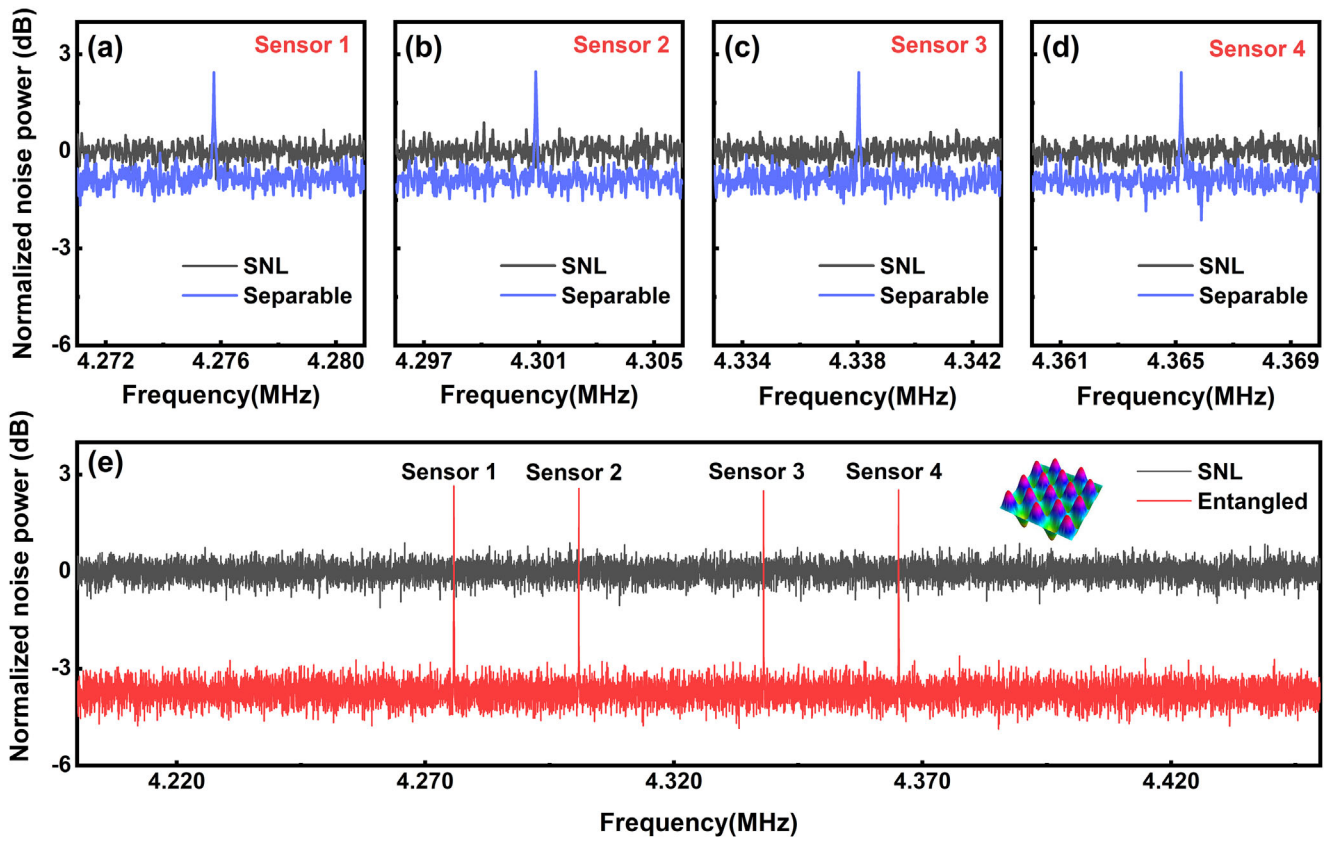


FIGURE 3 | Entanglement-induced imprecision noise reduction. Normalized power spectral densities (PSDs) of individual (a–d) and joint (e) homodyne measurement for membrane-based optomechanical sensors, where all the shot-noise PSDs (black curves) are normalized to unity. Each curve is averaged over 50 experimental traces acquired with the resolution bandwidth of 10 Hz and the video bandwidth of 1 Hz. Inset: the spatial shape of the (5,6) mode.

four BHD signals from optomechanical sensor network. The black curve denotes the joint SNL normalized to unity. The red curve, which encompasses four unaltered and traceable (5,6) mechanical modes from the optomechanical sensor network, is the joint homodyne PSD of four submodes. Crucially, due to the entangled characteristic among four submodes, the joint imprecision noise floor in the off-resonant region is reduced by up to ≈ 3.7 dB, corresponding to a 57.3% quantum advantage over coherent probes. In addition, the effective mechanical decay rate Γ_{eff} with entangled probes is $\Gamma_e = 45$ Hz by fitting the measured noise PSD (see Supporting Information Section S4), exhibiting a 10% reduction compared to that with coherent probes $\Gamma_e = 50$ Hz (not shown in Figure 3).

Similarly, we can also obtain the PSDs at two and three sensors in the cases of individual and joint homodyne measurement. Following these measurement results, we calculate the root-mean-square error (RMSE) for the entangled scenario σ_{η}^E , and compare with the separable scheme σ_{η}^S , shown in Figure 4a (see Supporting Information Section S2). The blue and red diamonds showcase experimental data with different number of sensors, and the error bars are obtained by taking into account the ± 0.2 dB fluctuation of the squeezed state. Especially with four optomechanical sensors, the RMSE are calculated as $\sigma_{0.82}^S = 0.160 \pm 0.002$ for the separable scheme and $\sigma_{0.82}^E = 0.130 \pm 0.002$ for the entangled approaches, respectively. The blue and red solid curves represent the theoretical fitting with a channel efficiency of 82.0%,

whereas the dotted curves correspond to 100% channel efficiency. When the number of sensors M exceeds one, the RMSE of the entangled sensor network consistently outperforms that of the separated scenario. Furthermore, the disparity in RMSE becomes more prominent with the increasing number of sensors.

Figure 4b systematically elucidates the DQS advantage ($\sigma_{\eta}^S/\sigma_{\eta}^E$) for the different number of sensors when employing joint measurement protocols. The purple squares highlight the experimental observable DQS advantages, and the purple solid curve is the theoretical fitting with 82% channel efficiency. For comparison, the purple dotted curve is the theoretical DQS advantage with 100% channel efficiency. With four optomechanical sensors, the experimentally obtained advantage is 23.7%, while the DQS advantage is approximately $\sqrt{4}$ -fold under perfect channel efficiency. For two and three sensors, the experimentally observed advantages are 8.9% and 17.8%, respectively, indicating that the DQS advantage becomes much more conspicuous with the increasing number of sensors. Therefore, the entangled sensor network is corroborated to have a scaling advantage over separable architectures, as shown in Figure 4b.

However, the observed DQS advantage is currently restricted by the initial squeezing parameter and 82% channel efficiency that includes propagation efficiency and detection efficiency. The initial squeezing parameter can be improved by increasing the escape efficiency of DROPA and improving the phase stability of

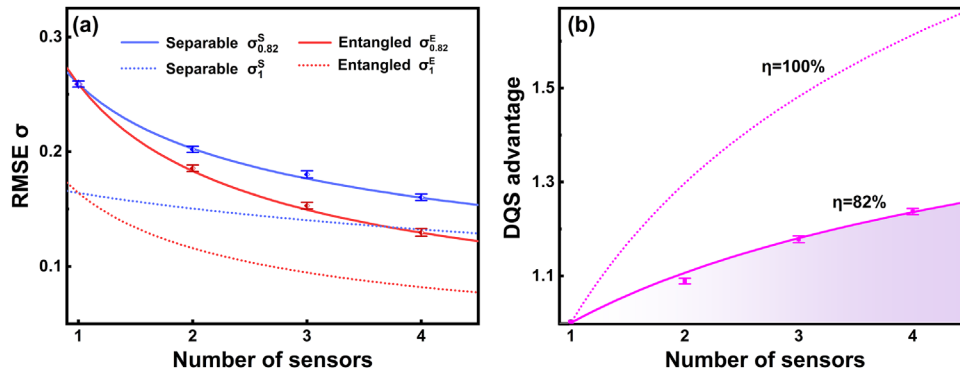


FIGURE 4 | Distributed quantum sensing advantage. Root-mean-square error (RMSE) (a) and DQS advantage (b) for different number of sensors. Data points are the experimental values within a moderate channel efficiency $\eta=82.0\%$ of our experimental setup. The gradient purple-filled region in the lower-right corner represents the DQS advantage.

the control loop. The 92% propagation efficiency can be optimized with ultralow-loss optical components, including dichroic mirror, half wave plate, polarization beam splitter and quarter wave plate. The 89% detection efficiency for each optomechanical sensor is limited by 99% quantum efficiency of photodiodes and 95% interference efficiency between each reflected probe and local oscillator, which can be improved by optimizing the spatial mode, spot size and position on the membrane. Any deviation from the perfect efficiency directly diminishes the potential quantum advantage, thereby broadening the disparity between the experimental and theoretical advantages. To mitigate the effects of system loss, future large-scale networks will require the integration of ultralow loss components, quantum repeaters and high-efficiency quantum memories.

4.2 | Entanglement-Enhanced Distributed Force Sensing

The entanglement enhanced distributed optomechanical sensor network is then applied to a more practical distribute sensing task that estimates incoherent forces, which refer to thermomechanical forces without a stable phase relationship over time in our experiment. Following the measurement results of Figure 3, we can calculate the force resolution $\sqrt{S_{F,j}(\omega)}$ for distributed force sensing with the expression (1), shown in Figure 5. For comparison, the black curves depict force resolution for coherent probes with the same laser power. The minimum force resolution 6.7 fN Hz^{-1/2} occurs at the mechanical resonance frequency, which is primarily limited by the dominant thermal noise S_{th} . This minimum force resolution could be further ulteriorly improved by integrating the optomechanical sensor network into a cryogenic, vacuum-compatible chamber. In the frequency region far away from resonance, the force resolution decreases to ≈ 197 fN Hz^{-1/2} due to the inherent characteristics of mechanical susceptibility $\chi(\omega)$.

For the separable scenario, the blue curves in Figure 5a–d correspond to the individual force resolutions respectively. The four minimum force resolutions reach ≈ 6.6 fN Hz^{-1/2}. The enhanced coupling strength, the reduced quantum fluctuation and the reduced mechanical decay rate collectively contribute

to a 1.5% improvement in force resolution compared to the coherent probe. In the frequency region far away from resonance, the force resolution reaches ≈ 184 fN Hz^{-1/2}, corresponding to a 6.6% enhancement relative to the coherent probe. The red solid curves in Figure 5e–h illustrate the entanglement enhanced force resolution. The minimum force resolution in the entangled scenario reaches ≈ 6.3 fN Hz^{-1/2}, which is improved by 4.5% compared to the separable scheme. In the far off-resonant region, the force resolution reaches ≈ 122 fN Hz^{-1/2}, due to the minimum quantum fluctuation and maximal coupling strength, achieving a 33.7% resolution enhancement. Utilizing the designed force resolution as reference, the corresponding inconsistencies of four optomechanical sensors are 2.4%, 2.3%, 1.6%, and 1.9%, respectively, all of which are below 3% (see Supporting Information Section S6). Moreover, the measured forces can be traced back to individual optomechanical sensor according to their distinct resonance frequencies, facilitating the operational status monitoring of each sensor.

In force sensing applications, one would expect to achieve unprecedented sensitivity operating on resonance, and reach the standard quantum limit (SQL), the level at which shot noise and back-action noise contribute equally to the total measurement results. Nevertheless, the resonance frequency of our optomechanical sensor is in the megahertz scale, thus the mean thermal occupancy number is $\approx 10^6$ orders at 300 K. With the optimum incident power (see Supporting Information Section S7) and perfect detection efficiency, the SQL at mechanical resonance frequency is expected to be achieved by cooling the optomechanical sensors to their ground state.

5 | Conclusion

In conclusion, we have successfully demonstrated a quantum-enhanced optomechanical sensor network with the shared four-partite entanglement state. Following the optomechanical sensor model, we addressed the challenge of poor uniformity that is one of the main limitations of scaling up the sensor network, yielding the four optomechanical sensors with the inconsistency of less than 2.4%. Integrated with high-performance squeezed state, it was the first time, to our knowledge, to demonstrate the quantum advantage of a maximum \sqrt{M} -fold increase trend with sensor

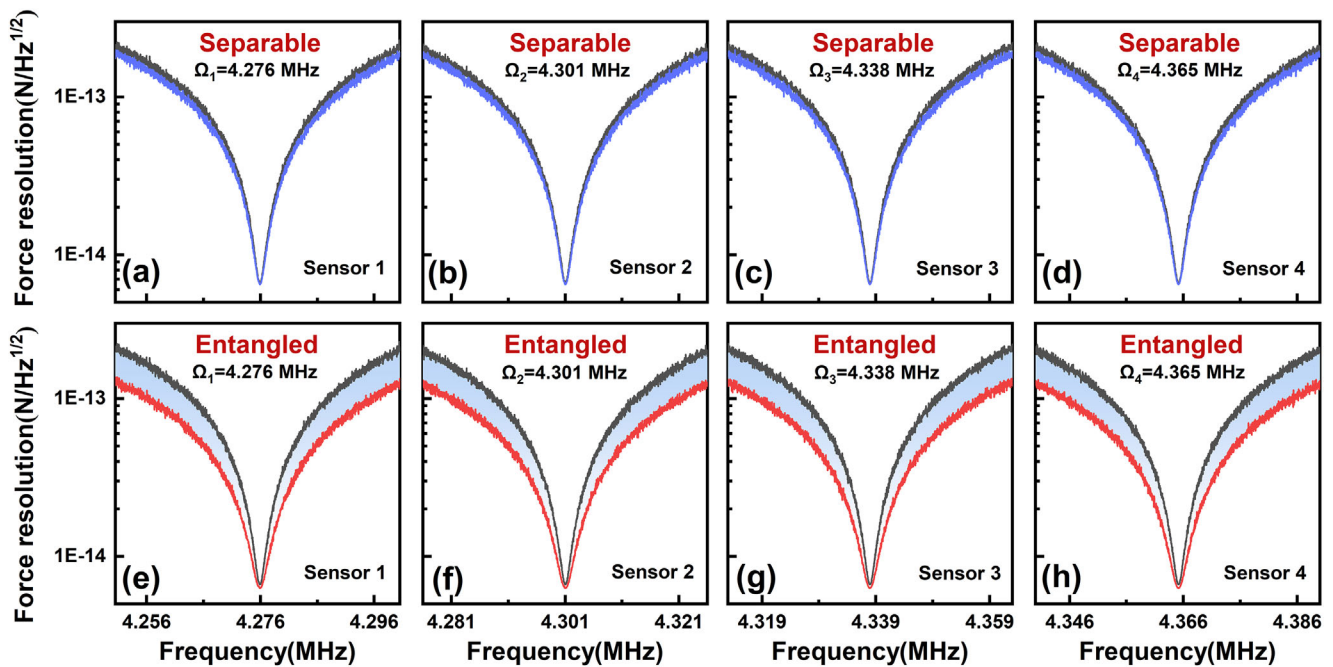


FIGURE 5 | Entanglement-enhanced distributed force sensing. Force resolution for distributed force sensing. The upper panels (a–d) show the individual force sensing of four sensors in the separable scenario, while the lower panels (e–h) depict the entanglement enhanced force sensing. The black, blue, and red curves represent the force resolution for coherent probe, separation scheme, and entanglement scenario, respectively. The blue gradient-shaded regions illustrate the quantum advantages of distributed force sensing.

number in a practical optomechanical sensor network. The quantum advantage of the optomechanical sensor network is 57.3% compared to that with coherent probes, and 23.7% compared to that with separable probes. The estimation precision showcases a trend toward Heisenberg scaling in moderate channel loss. In the incoherent force estimation task, the force resolution with sensor network achieves a 33.7% enhancement in contrast with the separable scheme. Crucially, we have addressed two main challenges of constraining network scale: uniformity of optomechanical sensors, squeezing parameter, expecting to drive the construction of a large-scale sensor network and achieve a more pronounced quantum advantage and richer physics.

6 | Experimental Section

The half-monolithic DROPA was composed of a concave output coupler and a periodically poled potassium titanyl phosphate (PPKTP) crystal. The output coupler, whose reflectance was 84.3% for the seed laser and 97.8% for the pump laser, had a radius of curvature of 25 mm. One end of the PPKTP crystal had a radius of curvature of 12 mm, and was highly reflective for both seed and pump lasers. The DROPA length was stabilized by pump laser with Pound–Drever–Hall technique, while the resonance condition for seed laser was realized by finely tuning the temperature of nonlinear crystal [85]. By controlling the relative phase between seed and pump laser to zero, a phase-squeezed state with $-7.1 \text{ dB} \pm 0.2 \text{ dB}$ noise reduction was generated [86]. The average photon number was calculated as $N_s = 2.3$.

The $500 \times 500 \mu\text{m}^2$ square Si_3N_4 membrane was fabricated by low-pressure chemical-vapor deposition (Norcada Inc.), and was

deposited on a $5 \times 5 \text{ mm}^2$ silicon wafer. The effective mass of Si_3N_4 membranes was $\approx 1.7 \times 10^{-11} \text{ kg}$. The mass density and tensile stress of the Si_3N_4 membrane was $\rho = 2.7 \text{ g cm}^{-3}$ and $T \approx 0.9 \text{ GPa}$, respectively. The reflectivity for 1550 nm laser was 30.2% when the thickness of membrane was 100 nm. According to the angular natural frequency for (m,n) mode $\Omega_{(m,n)} = 2\pi \sqrt{T(m^2 + n^2)/4l^2}$, the resonance frequency for $(5,6)$ mechanical mode was $\Omega_{(5,6)}/2\pi \approx 4.3 \text{ MHz}$.

Acknowledgements

Q.L. and W.L. contributed equally to this work. This work was supported by the National Natural Science Foundation of China (NSFC) (Grant Nos. 62225504, 12274275, 62027821, U22A6003, 62035015, 62375162, 12304399, 12174234); Key R&D Program of Shanxi (Grant No. 202302150101004).

Conflict of Interest

The authors declare no conflict of interest.

Data Availability Statement

The data that support the findings of this study are available from the corresponding author upon reasonable request.

References

1. V. Giovannetti, S. Lloyd, and L. Maccone, “Quantum Metrology,” *Physical Review Letters* 96 (2006): 010401.
2. V. Giovannetti, S. Lloyd, and L. Maccone, “Advances in Quantum Metrology,” *Nature Photonics* 5 (2011): 222–229.
3. M. Zwierz, C. A. Pérez-Delgado, and P. Kok, “General Optimality of the Heisenberg Limit for Quantum Metrology,” *Physical Review Letters* 105 (2010): 180402.

4. V. Giovannetti, S. Lloyd, and L. Maccone, "Quantum-Enhanced Measurements: Beating the Standard Quantum Limit," *Science* 306 (2004): 1330–1336.
5. B. M. Escher, R. L. de Matos Filho, and L. Davidovich, "General Framework for Estimating the Ultimate Precision Limit in Noisy Quantum-Enhanced Metrology," *Nature Physics* 7 (2011): 406–411.
6. C. Hotter, H. Ritsch, and K. Gietka, "Combining Critical and Quantum Metrology," *Physical Review Letters* 132 (2024): 060801.
7. D. R. Glenn, D. B. Bucher, J. Lee, M. D. Lukin, H. Park, and R. L. Walsworth, "High-Resolution Magnetic Resonance Spectroscopy Using a Solid-State Spin Sensor," *Nature* 555 (2018): 351–354.
8. S. Barzanjeh, A. Xuereb, S. Gröblacher, M. Paternostro, C. A. Regal, and E. M. Weig, "Optomechanics for Quantum Technologies," *Nature Physics* 18 (2022): 15–24.
9. Z. Meng, L. Wang, W. Han, et al., "Atomic Bose–Einstein Condensate in Twisted-Bilayer Optical Lattices," *Nature* 615 (2023): 231–236.
10. D. DeMille, N. Hutzler, A. Rey, and T. Zelevinsky, "Quantum Sensing and Metrology for Fundamental Physics with Molecules," *Nature Physics* 20 (2024): 741–749.
11. M. Yap, J. Cripe, G. L. Mansell, et al., "Broadband Reduction of Quantum Radiation Pressure Noise via Squeezed Light Injection," *Nature Photonics* 14 (2020): 19–23.
12. H. Yonezawa, D. Nakane, T. A. Wheatley, et al., "Quantum-Enhanced Optical-Phase Tracking," *Science* 337 (2012): 1514–1517.
13. B. J. Lawrie, P. D. Lett, A. M. Marino, and R. C. Pooser, "Quantum Sensing with Squeezed Light," *ACS Photonics* 6 (2019): 1307–1318.
14. J. Lough, E. Schreiber, F. Bergamin, et al., "First Demonstration of 6 dB Quantum Noise Reduction in a Kilometer Scale Gravitational Wave Observatory," *Physical Review Letters* 126 (2021): 041102.
15. W. Jia, V. Xu, K. Kuns, et al., "Squeezing the Quantum Noise of a Gravitational-Wave Detector Below the Standard Quantum Limit," *Science* 385 (2024): 1318–1321.
16. L. Kleybolte, P. Gewecke, A. Sawadsky, M. Korobko, and R. Schnabel, "Squeezed-Light Interferometry on a Cryogenically Cooled Micromechanical Membrane," *Physical Review Letters* 125 (2020): 213601.
17. B. B. Li, J. Bilek, U. B. Hoff, et al., "Quantum Enhanced Optomechanical Magnetometry," *Optica* 5 (2018): 850–856.
18. M. A. Taylor, J. Janousek, V. Daria, et al., "Biological Measurement Beyond the Quantum Limit," *Nature Photonics* 7 (2013): 229–233.
19. Y. Xia, A. R. Agrawal, C. M. Pluchar, et al., "Entanglement-Enhanced Optomechanical Sensing," *Nature Photonics* 17 (2023): 470–477.
20. R. C. Pooser, N. Savino, E. Batson, J. L. Beckey, J. Garcia, and B. J. Lawrie, "Truncated Nonlinear Interferometry for Quantum-Enhanced Atomic Force Microscopy," *Physical Review Letters* 124 (2020): 230504.
21. J. B. Clark, F. Lecocq, R. W. Simmonds, J. Aumentado, and J. D. Teufel, "Observation of Strong Radiation Pressure Forces From Squeezed Light on a Mechanical Oscillator," *Nature Physics* 12 (2016): 683–687.
22. Z. Liu, D. H. Xu, Y. J. Yang, and C. S. Yu, "Enhanced Sensing by Geometric Tuning of YIG Spheres: Noise Reduction, Signal Amplification, and Directional Magnetic-Field Detection," *Physical Review A* 111 (2025): 063706.
23. S. D. Zhang, J. Wang, Q. Zhang, et al., "Squeezing-Enhanced Quantum Sensing with Quadratic Optomechanics," *Optica Quantum* 2 (2024): 222–229.
24. T. P. Purdy, P. L. Yu, R. W. Peterson, N. S. Kampel, and C. A. Regal, "Strong Optomechanical Squeezing of Light," *Physical Review X* 3 (2013): 031012.
25. G. Huang, A. Beccari, N. J. Engelsens, and T. J. Kippenberg, "Room-Temperature Quantum Optomechanics Using an Ultralow Noise Cavity," *Nature* 626 (2024): 512–516.
26. S. Marti, U. von Lüpke, O. Joshi, et al., "Quantum Squeezing in a Nonlinear Mechanical Oscillator," *Nature Physics* 20 (2024): 1448–1453.
27. M. Korobko, Y. Ma, Y. Chen, and R. Schnabel, "Quantum Expander for Gravitational-Wave Observatories," *Light: Science & Applications* 8 (2019): 118.
28. S. L. Chao, Z. H. Li, and X. Y. Lü, "Enhancing Force Sensing in a Squeezed Optomechanical System with Quantum Nondemolition Measurement," *Communications in Theoretical Physics* 76 (2024): 015104.
29. S. K. Singh, M. Mazaheri, J. X. Peng, A. Sohail, M. Khalid, and M. Asjad, "Enhanced Weak Force Sensing Based on Atom-Based Coherent Quantum Noise Cancellation in a Hybrid Cavity Optomechanical System," *Frontiers in Physics* 11 (2023): 1142452.
30. W. Zhao, S. D. Zhang, A. Miranowicz, and H. Jing, "Weak-Force Sensing with Squeezed Optomechanics," *Science China Physics, Mechanics & Astronomy* 63 (2020): 224211.
31. F. Deng, S. Wei, Y. Xu, and H. Li, "Damage Identification of Long-Span Bridges Based on the Correlation of Monitored Global Dynamic Responses in High Dimensional Space," *Engineering Structures* 299 (2024): 117134.
32. B. Zerouali, Y. Sahraoui, M. Nahal, and A. Chateaneuf, "Reliability-Based Maintenance Optimization of Long-Distance Oil and Gas Transmission Pipeline Networks," *Reliability Engineering & System Safety* 249 (2024): 110236.
33. R. Tang, C. Sun, K. Bao, et al., "High-Resolution 2D Quasi-Distributed Optical Sensing with On-Chip Multiplexed FSR-Free Nanobeam Cavity Array," *Laser & Photonics Reviews* 18 (2024): 2300828.
34. A. Zadok, Y. Antman, N. Primerov, A. Denisov, J. Sancho, and L. Thevenaz, "Random-Access Distributed Fiber Sensing," *Laser & Photonics Reviews* 6 (2012): L1–L5.
35. M. S. Mrozowski, A. S. Bell, P. F. Griffin, et al., "Distributed Network of Optically Pumped Magnetometers for Space Weather Monitoring," *Scientific Reports* 14 (2024): 28229.
36. Z. Zhang, C. You, O. S. Magaña-Loaiza, et al., "Entanglement-Based Quantum Information Technology: a Tutorial," *Advances in Optics and Photonics* 16 (2024): 60–162.
37. Z. Zhang and Q. Zhuang, "Distributed Quantum Sensing," *Quantum Science and Technology* 6 (2021): 043001.
38. Y. Yang, B. Yadin, and Z. Xu, "Quantum-Enhanced Metrology with Network States," *Physical Review Letters* 132 (2024): 210801.
39. M. Gessner, A. Smerzi, and L. Pezzè, "Multiparameter Squeezing for Optimal Quantum Enhancements in Sensor Networks," *Nature Communications* 11 (2020): 3817.
40. T. J. Proctor, P. A. Knott, and J. A. Dunningham, "Multiparameter Estimation in Networked Quantum Sensors," *Physical Review Letters* 120 (2018): 080501.
41. M. Gessner, L. Pezzè, and A. Smerzi, "Sensitivity Bounds for Multiparameter Quantum Metrology," *Physical Review Letters* 121 (2018): 130503.
42. W. Ge, K. Jacobs, Z. Eldredge, A. V. Gorshkov, and M. Foss-Feig, "Distributed Quantum Metrology with Linear Networks and Separable Inputs," *Physical Review Letters* 121 (2018): 043604.
43. H. Kwon, Y. Lim, L. Jiang, H. Jeong, and C. Oh, "Quantum Metrological Power of Continuous-Variable Quantum Networks," *Physical Review Letters* 128 (2022): 180503.
44. Y. Xia, W. Li, W. Clark, D. Hart, Q. Zhuang, and Z. Zhang, "Demonstration of a Reconfigurable Entangled Radio-Frequency Photonic Sensor Network," *Physical Review Letters* 124 (2020): 150502.
45. X. Sun, W. Li, Y. Tian, et al., "Quantum Positioning and Ranging via a Distributed Sensor Network," *Photonics Research* 10 (2022): 2886–2892.
46. W. Li, X. Sun, Y. Tian, et al., "Quantum-Enhanced Angle-of-Arrival Pre-Estimation of Radio-Frequency Signals," *Optics and Laser Technology* 166 (2023): 109643.

47. X. Guo, C. R. Breum, J. Borregaard, et al., “Distributed Quantum Sensing in a Continuous-Variable Entangled Network,” *Nature Physics* 16 (2020): 281–284.
48. B. K. Malia, Y. F. Wu, J. Martínez-Rincón, and M. A. Kasevich, “Distributed Quantum Sensing with Mode-Entangled Spin-Squeezed Atomic States,” *Nature* 612 (2022): 661–665.
49. L. Liu, Y. Zhang, Z. Li, et al., “Distributed Quantum Phase Estimation with Entangled Photons,” *Nature Photonics* 15 (2021): 137–142.
50. S. Zhao, Y. Zhang, W. Liu, et al., “Field Demonstration of Distributed Quantum Sensing Without Post-Selection,” *Physical Review X* 11 (2021): 031009.
51. D. H. Kim, S. Hong, Y. Kim, et al., “Distributed Quantum Sensing of Multiple Phases with Fewer Photons,” *Nature Communications* 15 (2024): 266.
52. J. Liu, X. Luo, Y. Yu, et al., “Creation of Memory–memory Entanglement in a Metropolitan Quantum Network,” *Nature* 629 (2024): 579–585.
53. S. Hong, J. Rehman, Y. Kim, et al., “Quantum Enhanced Multiple-Phase Estimation with Multi-Mode N00N States,” *Nature Communications* 12 (2021): 5211.
54. A. Brady, X. Chen, Y. Xia, et al., “Entanglement-Enhanced Optomechanical Sensor Array with Application to Dark Matter Searches,” *Communications Physics* 6 (2023): 237.
55. Y. Xia, Q. Zhuang, W. Clark, and Z. Zhang, “Repeater-Enhanced Distributed Quantum Sensing Based on Continuous-Variable Multipartite Entanglement,” *Physical Review A* 99 (2019): 012328.
56. Q. Zhuang, J. Preskill, and L. Jiang, “Distributed Quantum Sensing Enhanced by Continuous-Variable Error Correction,” *New Journal of Physics* 22 (2020): 022001.
57. Y. Xia, W. Li, Q. Zhuang, and Z. Zhang, “Quantum-Enhanced Data Classification with a Variational Entangled Sensor Network,” *Physical Review X* 11 (2021): 021047.
58. B. Li, L. Ou, Y. Lei, and Y. Liu, “Cavity Optomechanical Sensing,” *Nanophotonics* 10 (2021): 2799.
59. U. A. Javid, S. D. Rogers, A. Graf, and Q. Lin, “Cavity Optomechanical Sensing in the Nonlinear Saturation Limit,” *Laser & Photonics Reviews* 15 (2021): 2100166.
60. B. P. Abbott, R. Abbott, T. D. Abbott, et al., “Observation of Gravitational Waves from a Binary Black Hole Merger,” *Physical Review Letters* 116 (2016): 061102.
61. B. P. Abbott, R. Abbott, T. D. Abbott, et al., “GW151226: Observation of Gravitational Waves From a 22-Solar-Mass Binary Black Hole Coalescence,” *Physical Review Letters* 116 (2016): 241103.
62. J. Cripe, N. Aggarwal, R. Lanza, et al., “Measurement of Quantum Back Action in the Audio Band at Room Temperature,” *Nature* 568 (2019): 364–367.
63. J. Chan, T. P. M. Alegre, A. H. Safavi-Naeini, et al., “Laser Cooling of a Nanomechanical Oscillator into its Quantum Ground State,” *Nature* 478 (2011): 89–92.
64. A. Krause, M. Winger, T. Blasius, Q. Lin, and O. Painter, “A High-Resolution Microchip Optomechanical Accelerometer,” *Nature Photonics* 6 (2012): 768–772.
65. Y. Huang, J. G. FlorFlores, Y. Li, et al., “A Chip-Scale Oscillation-Mode Optomechanical Inertial Sensor Near the Thermodynamical Limits,” *Laser & Photonics Reviews* 14 (2020): 1800329.
66. J. G. Flor Flores, T. Yerebakan, W. Wang, et al., “Parametrically Driven Inertial Sensing in Chip-Scale Optomechanical Cavities at the Thermodynamical Limits with Extended Dynamic Range,” *Laser & Photonics Reviews* 17 (2023): 2200827.
67. M. Sansa, M. Defoort, A. Brenac, et al., “Optomechanical Mass Spectrometry,” *Nature Communications* 11 (2020): 3781.
68. S. Forstner, S. Prams, J. Knittel, et al., “Cavity Optomechanical Magnetometer,” *Physical Review Letters* 108 (2012): 120801.
69. G. L. Zhu, J. Liu, Y. Wu, and X. Y. Lü, “Quantum Magnetometer with Dual-Coupling Optomechanics,” *Laser & Photonics Reviews* 16 (2022): 2100636.
70. R. E. Anthony, A. T. Ringler, and D. C. Wilson, “Improvements in Absolute Seismometer Sensitivity Calibration Using Local Earth Gravity Measurement,” *Bulletin of the Seismological Society of America* 108 (2019): 503–510.
71. F. Walter, D. Gräff, F. Lindner, et al., “Distributed Acoustic Sensing of Microseismic Sources and Wave Propagation in Glaciated Terrain,” *Nature Communications* 11 (2020): 2436.
72. A. Sladen, D. Rivet, J. P. Ampuero, et al., “Distributed Sensing of Earthquakes and Ocean-Solid Earth Interactions on Seafloor Telecom Cables,” *Nature Communications* 10 (2019): 5777.
73. E. F. Williams, M. R. Fernández-Ruiz, R. Magalhaes, et al., “Distributed Sensing of Microseisms and Teleseisms with Submarine Dark Fibers,” *Nature Communications* 10 (2019): 5778.
74. N. El-Sheimy and A. Youssef, “Inertial Sensors Technologies for Navigation Applications: State of the Art and Future Trends,” *Satellite Navigation* 1 (2020): 2.
75. J. Manley, M. D. Chowdhury, D. Grin, S. Singh, and D. J. Wilson, “Searching for Vector Dark Matter with an Optomechanical Accelerometer,” *Physical Review Letters* 126 (2021): 061301.
76. S. Shi, L. Tian, Y. Wang, Y. Zheng, C. Xie, and K. Peng, “Demonstration of Channel Multiplexing Quantum Communication Exploiting Entangled Sideband Modes,” *Physical Review Letters* 125 (2020): 070502.
77. S. Shi, Y. Wang, L. Tian, et al., “Continuous Variable Quantum Teleportation Network,” *Laser & Photonics Reviews* 17 (2023): 2200508.
78. L. Gao, L. Zheng, B. Lu, S. Shi, L. Tian, and Y. Zheng, “Generation of Squeezed Vacuum State in the Millihertz Frequency Band,” *Light: Science & Applications* 13 (2024): 294.
79. Y. Tian, Y. Wang, W. Wang, et al., “Reservoir-Engineered Squeezed Lasing Through the Parametric Coupling,” *Physical Review Letters* 134 (2025): 243803.
80. X. Su, A. Tan, X. Jia, J. Zhang, C. Xie, and K. Peng, “Experimental Preparation of Quadripartite Cluster and Greenberger-Horne-Zeilinger Entangled States for Continuous Variables,” *Physical Review Letters* 98 (2007): 070502.
81. X. Liu, S. Shi, Y. Wu, et al., “Continuous Variable Quantum Communication with 40 Pairs of Entangled Sideband Modes,” *Science China Physics, Mechanics & Astronomy* 68 (2025): 124211.
82. K. Zhang, W. Wang, S. Liu, et al., “Reconfigurable Hexapartite Entanglement by Spatially Multiplexed Four-Wave Mixing Processes,” *Physical Review Letters* 124 (2020): 090501.
83. Q. Zhuang, Z. Zhang, and J. H. Shapiro, “Distributed Quantum Sensing Using Continuous-Variable Multipartite Entanglement,” *Physical Review A* 97 (2018): 032329.
84. D. Mason, J. Chen, M. Rossi, Y. Tsaturyan, and A. Schliesser, “Continuous Force and Displacement Measurement Below the Standard Quantum Limit,” *Nature Physics* 15 (2019): 745–749.
85. Y. Sun, Y. Tian, Y. Wang, et al., “Squeezing Level Strengthened by a Temperature Dependent Dispersion Compensation Methodology,” *Optics Communications* 530 (2023): 129192.
86. W. Li, M. Ju, Q. Li, et al., “Squeezing-Enhanced Resolution of Radio-Frequency Signals,” *Chinese Optics Letters* 22 (2024): 072701.

Supporting Information

Additional supporting information can be found online in the Supporting Information section.

Supporting Information